DOI: 10.1002/anie.201101213

VIP Composite Nanomaterials

Nanocomposites of Ag_2S and Noble Metals**

Jun Yang and Jackie Y. Ying**

Besides the more conventional hybrid nanomaterials, for example, core–shell,[1–4] alloy,[5–7] and bimetallic heterostructures,[8–11] there has been increasing interest devoted towards the development of semiconductor–metal nanocomposites that consist of different classes of materials with coherent interfaces. This type of nanostructure combines materials with distinctly different physical and chemical properties to yield a unique hybrid nanosystem with multifunctional capabilities and tunable or enhanced properties that may not be attainable otherwise.[12]

The early studies of semiconductor–metal nanocomposites involved different metals (e.g. gold, silver, and platinum) deposited on or doped in TiO_2 powders for photocatalytic applications.[13–19] In these structures, the metal domain induces the charge equilibrium in photoexcited TiO_2 nanocrystals, thus affecting the energetics of the nanocomposites by shifting the Fermi level to more negative potentials. The shift in Fermi level is indicative of improved charge separation in TiO_2–metal systems and is effective towards enhancing the efficiency of photocatalysis.[20,21]

In 2004, Banin and co-workers made a breakthrough in semiconductor–metal nanocomposites.[22] They demonstrated a solution synthesis for nanohybrids by the selective growth of gold tips on the apexes of hexagonal-phase CdSe nanorods at room temperature. The novel nanostructures displayed modified optical properties arising from the strong coupling between the gold and semiconductor components. The gold tips showed increased conductivity and selective chemical affinity for forming self-assembled chains of rods. The architecture of these nanostructures was qualitatively similar to bifunctional molecules such as dithiols, which provide two-sided chemical connectivity for self-assembly and for electrical devices and contacting points for colloidal nanorods and tetrapods. These researchers later reported the synthesis of asymmetric semiconductor–metal heterostructures in which gold was grown on one side of CdSe nanocrystalline rods and dots. Theoretical modeling and experimental analysis showed that the one-sided nanocomposites were transformed from the two-sided architectures through a ripening process.[23] Subsequently, various approaches were developed for the synthesis of semiconductor–metal nanocomposites (e.g. ZnO–Ag,[24,25] CdS–Au,[26,27] InAs–Au,[28] TiO_2–Co,[29] PbS–Au,[30–34] Ag_2S–Au,[35] and semiconductor–Pt systems[36–39]) by anisotropic growth of metals on semiconductors through reduction, physical deposition, or photochemistry.

We recently presented a general protocol for transferring the transition-metal ions from water to an organic medium using an ethanol-mediated method, which was extended to synthesize a wide variety of heterogeneous semiconductor–noble-metal nanocomposites.[40] In another study, we synthesized three different types of semiconductor–Au nanocomposites (CdS–Au, CdSe–Au, and PbS–Au), which displayed attractive catalytic activities in the three-component coupling reaction of benzaldehyde, piperidine, and phenylacetylene in water. Through electronic coupling between semiconductor and gold domains, PbS–Au nanocomposites provided superior catalytic activity, giving the desired propargylic amine as isolated product in yields of up to 95%.[41] Herein we report a facile, aqueous route to synthesize nanocomposites consisting of Ag_2S and different noble metals for direct methanol fuel cell (DMFC) applications. In this approach, Ag_2S nanocrystals with an average diameter of 7 nm were used as seeds for the growth of different noble metals upon the reduction of various metal precursors by citrate in aqueous solution.

A room-temperature method was developed to first derive aqueous-dispersible Ag_2S nanocrystals. Typically, bis(*p*-sulfonatophenyl)phenylphosphane dihydrate dipotassium salt (BSPP, 600 mg) was added to aqueous $AgNO_3$ solution (1 mM, 300 mL) in a 1000 mL beaker. The mixture was stirred for 1 h to form BSPP–Ag^I complexes, with subsequent prompt addition of aqueous Na_2S solution (50 mM, 10 mL), which resulted in a series of color changes before finally a brown Ag_2S hydrosol was produced. A transmission electron microscopy (TEM) image of the as-prepared Ag_2S nanocrystals is shown in Figure 1a. The nanocrystals were spherical, nearly monodispersed, and had an average diameter of 7.2 nm. The high-resolution TEM (HRTEM) image (Figure 1b) illustrated the lattice planes in these nanocrystals, showing an interplanar spacing of approximately 0.26 nm, which corresponded to the $(\bar{1}21)$ planes of monoclinic Ag_2S. The successful synthesis of monoclinic Ag_2S nanocrystals was confirmed by the powder X-ray diffraction

[*] Prof. J. Yang, Prof. J. Y. Ying
Institute of Bioengineering and Nanotechnology
31 Biopolis Way, The Nanos, Singapore 138669 (Singapore)
Fax: (+65) 6478-9080
E-mail: jyying@ibn.a-star.edu.sg
Prof. J. Yang
Institute of Process Engineering, Chinese Academy of Sciences
Beijing, 100190 (China)
Fax: (+86) 10-8254-4915
E-mail: jyang@mail.ipe.ac.cn

[**] We thank Dr. Jinhua Yang (Institute of Bioengineering and Nanotechnology (IBN)) for his assistance with the electrochemical measurements and Dr. Jiang Jiang, Dr. Yuangang Zheng, Dr. Jianping Xie, and Dr. Xiaojun Chen (IBN) for helpful discussions. We are grateful to Prof. Jim Yang Lee (National University of Singapore) for the use of the XPS facilities. This work was supported by IBN (Biomedical Research Council, Agency for Science, Technology and Research, Singapore). Part of the characterizations was completed at the Institute of Process Engineering, Chinese Academy of Sciences.

Supporting information for this article is available on the WWW under http://dx.doi.org/10.1002/anie.201101213.

© 2011 Wiley-VCH Verlag GmbH & Co. KGaA, Weinheim

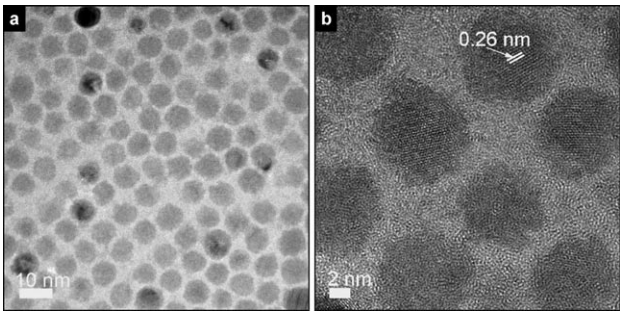

Figure 1. a) TEM and b) HRTEM images of the as-prepared Ag_2S nanocrystals. $d_{av} = 7.2$ nm, $\sigma = 0.6$ nm, $\bar{\sigma} = 8.4\%$. σ and $\bar{\sigma}$ are the standard derivation and relative standard derivation, respectively.

(XRD) pattern (Supporting Information Figure S1, JCPDS 140072).

The Ag_2S nanocrystals were then used as seeds for the formation of nanocomposites with different metals. Sodium citrate was added to the Ag_2S hydrosol as a reducing agent at reflux, and subsequently various noble-metal precursors were introduced. The reaction temperature was controlled at 105 °C for gold and 110 °C for other noble metals. Under these experimental conditions, metals nucleated preferentially on the existing Ag_2S nanocrystals rather than homogeneously. The nanocomposites obtained are illustrated in Figure 2. The deposition of noble metals on the Ag_2S nanocrystals was clearly identified by brightness contrast and confirmed by the energy-dispersive X-ray (EDX) spectroscopy analysis of an arbitrary single particle with high-angle annular dark-field scanning transmission electron microscopy (HAADF-STEM). Notably, in the absence of Ag_2S nanoparticles, the reduction of Pd or Os precursors by citrate in the aqueous phase was not possible, thus indicating that Ag_2S nanocrystals acted as catalysts for the reduction process, analogous to the reduction of Au^{III} ions catalyzed by Ag_2S or PbS in toluene.[32,35]

Figure 2 illustrates that gold was deposited only at a single site on each Ag_2S nanocrystal, whereas the nucleation and growth of Pt and Os occurred at multiple sites on each Ag_2S nanocrystal. Unlike the reported CdSe–Au[22] and PbS–Au[31] systems, changes in metal-precursor / Ag_2S ratio did not alter the morphology of the semiconductor–noble-metal nanocomposites but resulted in changes in the metal domain size on each Ag_2S nanocrystal (see Figure 2 and Supporting Information Figures S2 and S3).

Ag_2S–Ir nanocomposites were analogous to Ag_2S–Pt and Ag_2S–Os nanocomposites (Supporting Information Figure S4). However, the nucleation of iridium on the Ag_2S nanocrystals usually induced the aggregation of the final composite products, resulting in the formation of Ag_2S–Ir nanonets.

The final morphology of the nanocomposites depended on whether the surface of substrate particles allowed for only a single nucleation site or for multiple ones. Unlike face-centered cubic (fcc) or hexagonal materials, monoclinic Ag_2S has very complicated crystal structures. It has many facets with different lattice spacings (see Supporting Information Table S1 for the lattice spacing of different planes of Ag_2S), which provided favorable sites to match the lattice planes of various noble metals for their epitaxial growth on the substrate seeds. This explanation has been used to account for the formation of Fe_3O_4–Au and PbS–Au hybrids[30] and of Pd–Pt heterostructures.[11] Our experimental results showed that only a single site on the Ag_2S nanocrystal surface was suitable for the nucleation of gold clusters, but multiple sites existed over the surface of Ag_2S seeds for Pt, Os, and Ir noble metals. An extreme case was observed with the Ag_2S–Pd system (Figure 2 m–p). Numerous sites were provided for the nucleation of Pd nanoparticles, which could grow and eventually coalesce to form a continuous shell on each Ag_2S nanocrystal. Analogous results were also noted in the Ag_2S–Rh system, for which the formation of a continuous Rh shell on each Ag_2S seed was clearly demonstrated by TEM and EDX elemental profiles (Supporting Information Figure S5).

The species-dependent features of noble-metal deposition on Ag_2S nanocrystals could be further employed to derive various semiconductor–metal nanocomposites. We have prepared complex Ag_2S–Au–Pt, Ag_2S–Au–Os, Ag_2S–Pt–Os, and Ag_2S–Au–Pt–Os semiconductor–metal nanocomposites by successive reduction of noble-metal precursors using citrate in the presence of preformed Ag_2S nanocrystals (Figure 3). By comparison to the images in Figure 2, the domains with enhanced contrast and larger particle size (ca. 3 nm) in the complex nanocomposites could be indexed to gold, whereas other noble metals in the same nanocomposites appeared as smaller dots (ca. 1 nm for Pt and Os). For the Ag_2S–Pt–Os system, as Pt and Os have similar domain sizes and both have similar imaging contrast to the Ag_2S substrate (Figure 3 i–k), it was difficult to differentiate the Pt and Os domains in the nanocomposite particles. The presence of Pt, Os, and Ag_2S in the nanocomposite particles was confirmed by the EDX analysis performed on an arbitrary particle under the HAADF-STEM mode (Figure 3 l and Supporting Information Figure S6). The growth of more than one type of metal on each Ag_2S nanocrystal demonstrated that the nucleation sites on the Ag_2S nanocrystal surface were specific to different metals, thus providing for the possibility of creating complex nanocomposites between Ag_2S and multiple metals by a simple and flexible route.

The Pt-containing Ag_2S–noble-metal nanocomposites were examined for their electrocatalytic activities towards the room-temperature methanol oxidation reaction (MOR). These complex nanocomposites were attractive for this important energy application owing to their relatively small Pt domain size in the nanocomposite systems. The smaller Pt crystallite size translated to a higher surface area, which would be beneficial to the catalytic reaction. The electrochemically active surface area (ECSA) of Pt in Pt-containing Ag_2S–noble-metal nanocomposites was determined using cyclic voltammetry and benchmarked against that in commercial Pt/C catalysts (E-ETK, 20 wt % Pt nanoparticles (3.2 nm) on Vulcan XC-72 carbon support; Supporting Information Figure S7). There were three distinct potential regions in the voltammgrams (Figure 4 a): the hydrogen adsorption/desorption region (−0.2–0.1 V vs. Ag/AgCl), the double-layer region (0.1–0.4 V), and the surface oxide (OH_{ads}) formation/stripping region (> 0.4 V).[42] The specific

 © 2011 Wiley-VCH Verlag GmbH & Co. KGaA, Weinheim

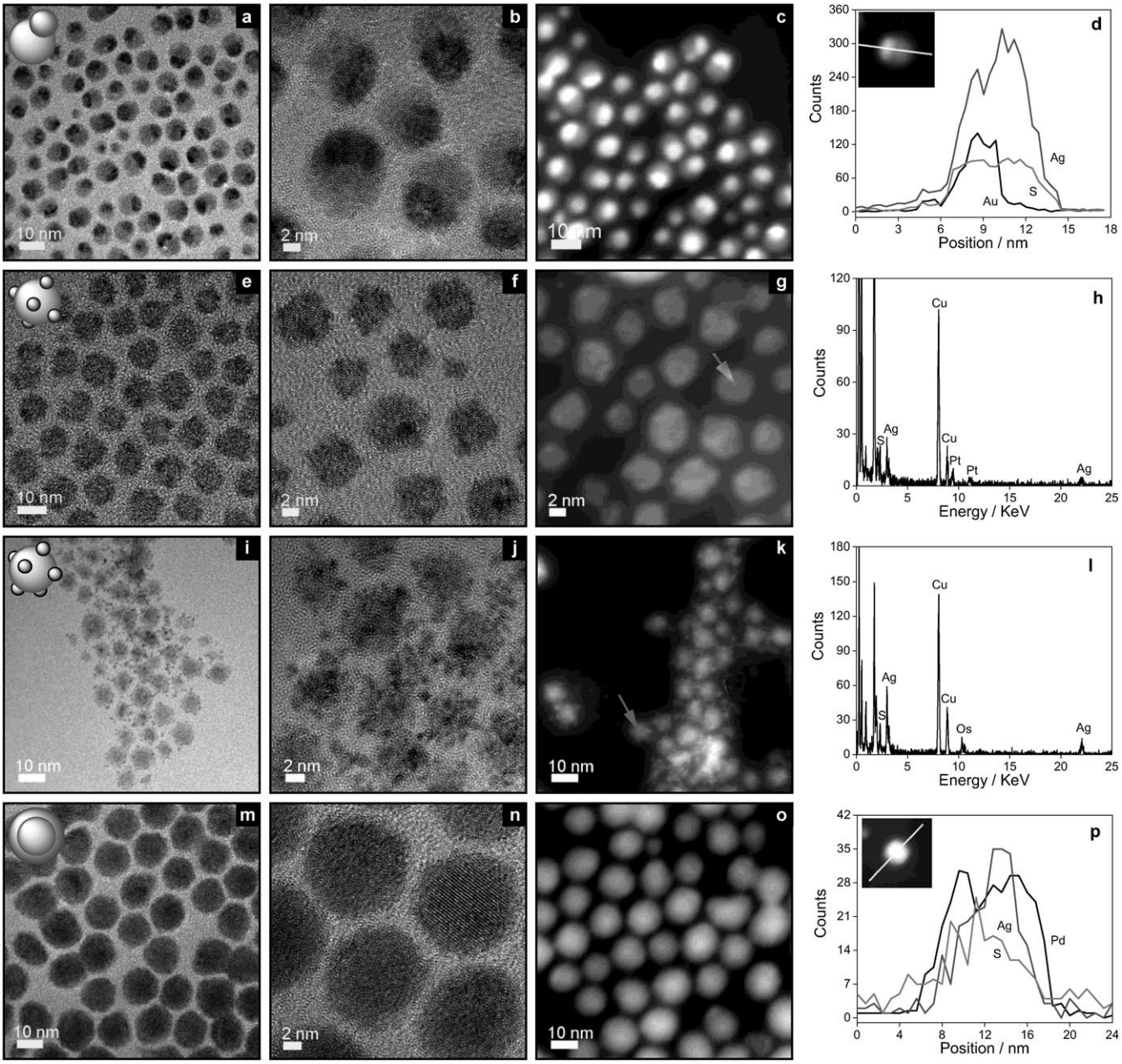

Figure 2. a) TEM, b) HRTEM, and c) HAADF-STEM images and d) Au, Ag, and S elemental profiles of Ag_2S–Au nanocomposites synthesized at a Au/Ag_2S precursor molar ratio of 1:1. A Au nanocrystal of approximately 3 nm diameter was deposited at a single site on each Ag_2S nanocrystal. e) TEM, f) HRTEM, and g) HAADF-STEM images and h) EDX analysis of Ag_2S–Pt nanocomposites synthesized at a Pt/Ag_2S precursor molar ratio of 1:1. Pt nanocrystals of approximately 1.1 nm diameter were deposited at multiple sites on each Ag_2S nanocrystal. i) TEM, j) HRTEM, and k) HAADF-STEM images and l) EDX analysis of Ag_2S–Os nanocomposites synthesized at an Os/Ag_2S precursor molar ratio of 1:1. Os nanocrystals of approximately 1.2 nm diameter were deposited at multiple sites on each Ag_2S nanocrystal. m) TEM, n) HRTEM, and o) HAADF-STEM images and p) Pd, Ag, and S elemental profiles of Ag_2S–Pd nanocomposites synthesized at a Pd/Ag_2S precursor molar ratio of 2:1. A continuous Pd shell was formed on each Ag_2S nanocrystal. The elemental profiles in (d) and (p) were obtained from EDX analysis along the white line across one nanocomposite particle (insets of d and p, respectively). The EDX analyses in (h) and (l) were performed on the one nanocomposite particle indicated by the arrows in (g) and (k), respectively.

ECSA, based on the unit weight of Pt and calculated by integrating the charge associated with the hydrogen adsorption/desorption potential region after double-layer correction, is summarized in the Supporting Information, Table S2. Although the coherent interfaces between Pt and Ag_2S in the nanocomposites resulted in some blockage of the surface area of the Pt domains, the ECSA of the Pt in Pt-containing Ag_2S–metal nanocomposites averaged 84.5 $m^2 g^{-1}$, which was 16% higher than that of the commercial Pt/C catalyst (72.9 $m^2 g^{-1}$) owing to the smaller Pt domain size of the former (ca. 1 nm).

The other important feature of the nanocomposites is the electronic coupling between the metal and semiconductor

 © 2011 Wiley-VCH Verlag GmbH & Co. KGaA, Weinheim

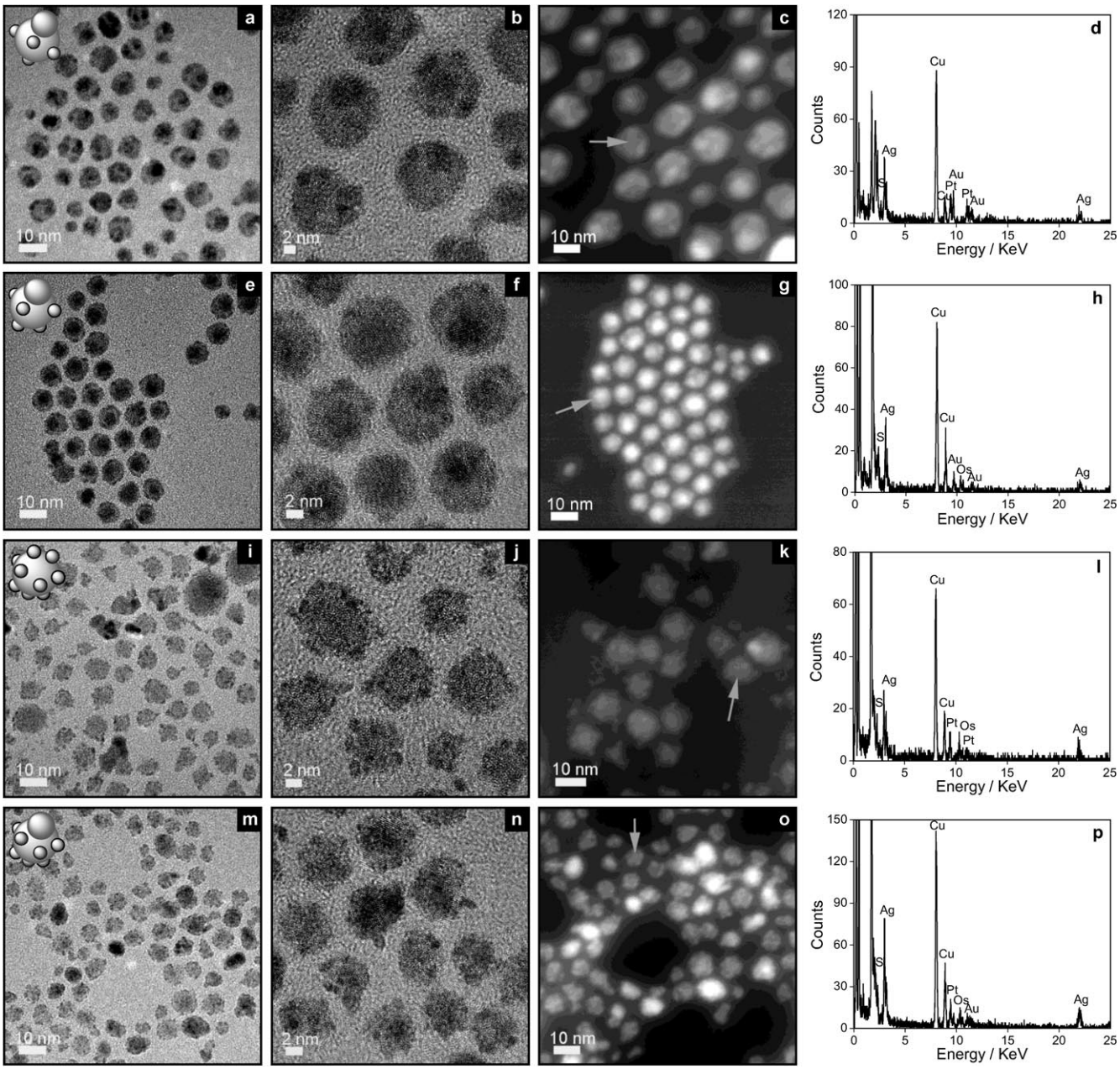

Figure 3. Complex Ag_2S–noble-metal nanocomposites prepared at a metal/Ag_2S precursor molar ratio of 1:1. a, e, i, m) TEM images; b, f, j, n) HRTEM images; c, g, k, o) HAADF-STEM images, and d, h, i, p) EDX analyses of a–d) Ag_2S–Au–Pt nanocomposites, e–h) Ag_2S–Au–Os nanocomposites, i–l) Ag_2S–Pt–Os nanocomposites, and m–p) Ag_2S–Au–Pt–Os nanocomposites. The EDX analysis was conducted on the one nanocomposite particle indicated by the arrow in (c, g, k, o).

domains. The X-ray photoelectron spectroscopy (XPS) Pt 4f spectra of the commercial Pt/C and Pt-containing Ag_2S–noble-metal nanocomposites were analyzed. Figure 4b shows that the Pt 4f spectra can be deconvoluted into two pairs of doublets. As shown in the Supporting Information, Table S3, the more intense doublet (at 71.0 and 74.3 eV for Pt/C, 70.6 and 73.9 eV for Ag_2S–Pt, 70.3 and 73.6 eV for Ag_2S–Au–Pt, 70.5 and 73.8 eV for Ag_2S–Pt–Os, 70.3 and 73.6 eV for Ag_2S–Au–Pt–Os) corresponded to Pt^0. The second and weaker doublet, with binding energies approximately 1.4 eV higher than those of Pt^0, could be assigned to Pt^{II} as in PtO and $Pt(OH)_2$.[43,44] Compared with the Pt $4f_{7/2}$ and $4f_{5/2}$ binding energies of commercial Pt/C catalysts, an appreciable shift to lower values was observed in the Pt-containing Ag_2S–noble-metal nanocomposites, thus suggesting that electrons were transferred to Pt from other domains of the nanocomposites. The comparison of the Pt 4f XPS spectra of Ag_2S–Au–Pt, Ag_2S–Au–Pt–Os, and other Pt-containing Ag_2S–metal nanocomposites (Ag_2S–Pt and Ag_2S–Pt–Os) further revealed that the presence of the Au domain could promote this electron-donating effect. The decrease in the Pt 4f binding energies was approximately 0.7 eV in Ag_2S–Au–Pt and Ag_2S–Au–Pt–Os nanocomposites and only 0.4–0.5 eV in Ag_2S–Pt and Ag_2S–Pt–Os nanocomposites. This electron-donating effect to

 © 2011 Wiley-VCH Verlag GmbH & Co. KGaA, Weinheim

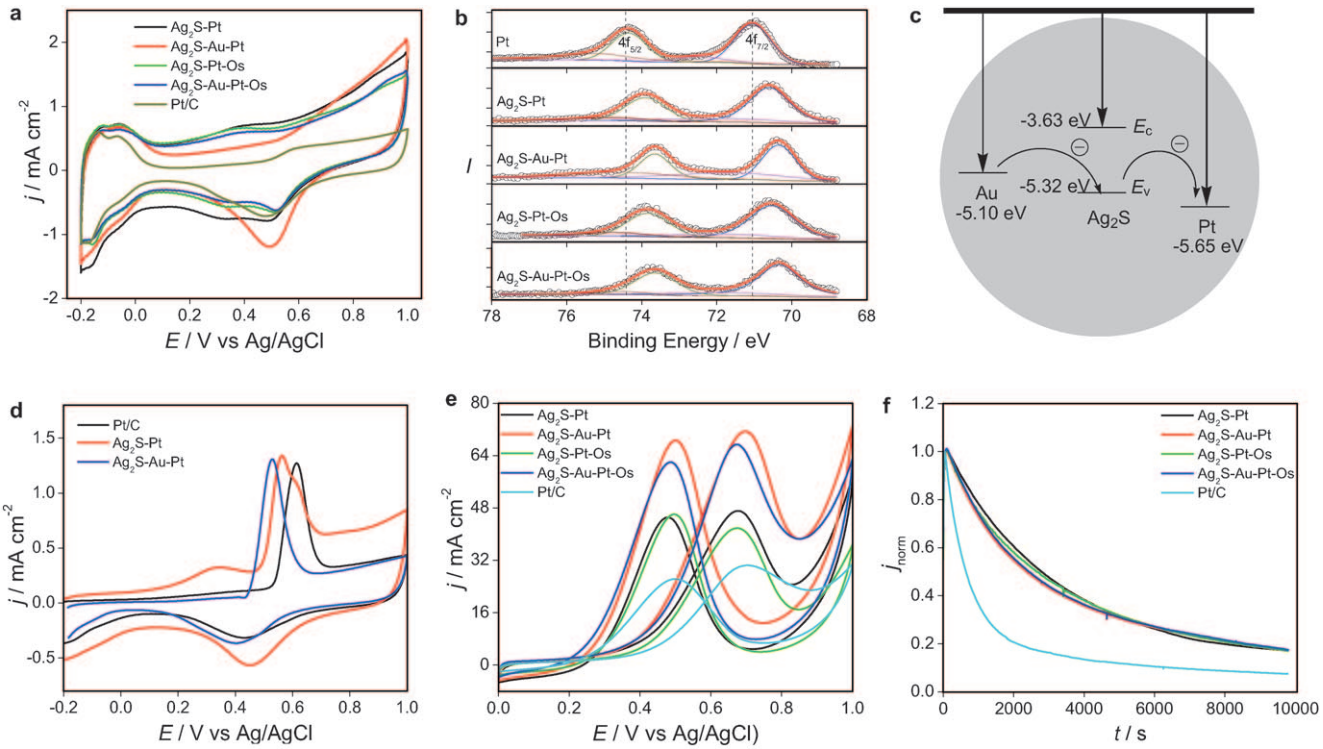

Figure 4. Characterization of Pt-containing Ag_2S–noble-metal nanocomposites. a) Cyclic voltammograms of Pt-containing nanocomposites in argon-purged $HClO_4$ (0.1 M) at room temperature. Sweep rate = 50 mV s^{-1}. b) Pt 4f XPS spectra of the Pt-containing Ag_2S–noble-metal nanocomposites. c) Energy-level diagram for Ag_2S–noble-metal nanocomposites, which predicts intraparticle charge transfer among different domains. E_c = energy of the conducting band, E_v = energy of the valence band. d) Room-temperature CO stripping from the commercial Pt/C catalyst and from Ag_2S–Pt and Ag_2S–Au–Pt nanocomposites in $HClO_4$ (0.1 M). e) Cyclic voltammograms of Pt-containing nanocomposites in argon-purged $HClO_4$ (0.1 M) with methanol (1 M). Sweep rate: 20 mV s^{-1}; room temperature. f) Chronoamperograms of Pt-containing nanocomposites at 0.45 V vs. Ag/AgCl at room temperature in argon-purged $HClO_4$ (0.1 M) with methanol (1 M).

Pt domains could be explained by intraparticle charge transfer (see Figure 4c for the energy-level diagram). Comparison of the electronic affinity of bulk Ag_2S (3.63 eV)[45] and the work function of Pt (5.65 eV)[46,47] predicted that the alignment of energy levels in Ag_2S and Pt would be favorable for electron transfer from Ag_2S to Pt. Analogous charge transfer has been observed in the Au@PbS system, whereby electron transfer from the PbS shell to the inner Au core resulted in the n-type to p-type change in hydrazine-treated PbS.[34] The electron transfer from Ag_2S to Pt could also be described with the generation of a hole in the Ag_2S domain. In the presence of a Au domain (work function = 5.1 eV),[46,47] the alignment of energy levels in Au and Ag_2S would be favorable for electron transfer from Au to Ag_2S to fill the hole generated by the electron transfer to Pt domains, further promoting the electron transfer from Ag_2S to Pt in order for the Fermi levels to match at the interface. The electron-donating effect from Au to Ag_2S has also been supported by the XPS analysis of the Au 4f region, whereby an appreciable shift in the 4f binding energies of Au in the nanocomposites to higher values was found as compared to the Au 4f binding energies of monometallic Au particles (Supporting Information Figure S8 and Table S4). On the other hand, the Os domains did not contribute to the electron donation from Ag_2S to Pt. The higher work function of Os (5.93 eV)[48] would inhibit the electron donation from Os to the neighboring Ag_2S domain.

Platinum is the most active metal for the dissociative adsorption of methanol. However, at room and moderate temperatures, it could be readily poisoned by carbon monoxide (CO), an intermediate product of methanol oxidation.[49] The nature of the Pt–CO bond in platinum systems has been well documented.[50] The chemisorption of CO on Pt involves the donation of an electron pair from the σ^* antibonding orbitals of CO to the unfilled 5d orbitals of Pt. A back donation of electrons from the Pt metal to the CO orbitals further stabilizes their interaction. Thus, the dative electron donation from CO to Pt is a prerequisite for strong CO chemisorption. Analogous to the electron donation from tin to platinum in the Pt–Sn system,[51] the charge transfer from Ag_2S to Pt in the Pt-containing Ag_2S–noble-metal nanocomposites (as evident in XPS studies) led to a substantial increase in the electron density around the Pt sites. This increase would result in the weaker chemisorption of CO and promote the MOR.

Figure 4d shows the CO stripping voltammograms of commercial Pt/C and two Pt-containing Ag_2S–metal nanocomposites (Ag_2S–Pt and Ag_2S–Au–Pt) after the working electrode has been held at −0.15 V for 30 min in CO-saturated 0.1 M $HClO_4$. The CO stripping peaks of the Pt-

 © 2011 Wiley-VCH Verlag GmbH & Co. KGaA, Weinheim

containing nanocomposites shifted to a more negative potential as compared to commercial Pt/C, thus indicating a more facile CO removal, and hence, an improved CO tolerance in practice. Moreover, the CO stripping peak of the Ag_2S–Au–Pt nanocomposite was located at a more negative potential than that of the Ag_2S–Pt nanocomposite, thus suggesting more facile CO removal from the Pt surfaces in the Ag_2S–Au–Pt system. The ease of CO removal over Ag_2S–Pt and Ag_2S–Au–Pt relative to commercial Pt/C reflected the effectiveness of electron coupling among the different domains in our nanocomposites.

Voltammograms of methanol oxidation were obtained in the potential window of 0–1 V at a swept rate of 20 $mV s^{-1}$ (Figure 4e). The current densities in the voltammograms were normalized by the ECSA of Pt. The voltammetric features were typical of methanol electrooxidation reported in the literature:[52] methanol oxidation commenced at approximately 0.3 V over the Pt catalysts, and a fully developed oxidation peak was formed at about 0.7 V. The peak current densities associated with methanol oxidation in the forward and reverse scans are summarized in the Supporting Information, Table S5. The comparison of current densities indicated that the Pt-containing nanocomposites showed greater specific activities than the commercial Pt/C nanoparticles, as expected. In particular, the Ag_2S–Au–Pt and Ag_2S–Au–Pt–Os nanocomposites displayed the highest catalytic activities for methanol oxidation. The enhanced catalytic activity of Ag_2S–metal nanocomposites could be attributed to the reasonably high surface area intrinsic to the finer Pt domains in our nanocomposites and to the electronic coupling between Pt and the other domains in the nanocomposites. The long-term performance of commercial Pt/C and Pt-containing Ag_2S–metal nanocomposites in methanol oxidation was illustrated in the chronoamperograms in Figure 4f. The slower rate of decay for the Pt-containing nanocomposites indicated their superior CO tolerance to the commercial Pt/C catalysts.

Contrary to their high catalytic activity for MOR, the Pt-containing Ag_2S–noble-metal nanocomposites exhibited poor activity for the oxygen reduction reaction (ORR), another key reaction in DMFC.[53] Polarization curves for the ORR over commercial Pt/C catalysts and Ag_2S–Pt and Ag_2S–Au–Pt nanocomposites are presented in the Supporting Information, Figure S9. Supporting Information Table S6 summarizes the ORR catalytic activities of these materials at room temperature. The half-wave potentials for Ag_2S–Pt and Ag_2S–Au–Pt were 460 and 360 mV, only 75 and 59%, respectively, of that of commercial Pt/C. The kinetic current density at the half-wave potential of nanocomposites was also lower than that of Pt/C. The poor catalytic activity of the nanocomposites for ORR was not surprising based on a report by Watanabe and co-workers,[54] which discussed alloying of iron, nickel, or cobalt with platinum to enhance the electrocatalytic activity for oxygen reduction. Iron, nickel, and cobalt have more 5d vacancies than platinum and could withdraw electrons from the latter. This electron-withdrawing effect induced an increase in 5d vacancies in Pt, thus increasing 2π electron donation from O_2 to the Pt surface and resulting in enhanced O_2 adsorption to favor oxygen reduction. However, for the Pt-containing Ag_2S–noble-metal nanocomposites, the electron donation from the semiconductor to the Pt domains would decrease the number of 5d vacancies in Pt. Thus, the adsorption of O_2 on the nanocomposites would be too weak for the O_2 dissociation reaction. This scenario would account for the poor activity of the Pt-containing nanocomposites towards ORR.

In summary, our studies elucidated a promising route for designing and deriving semiconductor–noble-metal nanocomposites with improved MOR activity by electron coupling among the different domains of hybrid materials. By optimizing both the composition and domain sizes for the nanocomposite system by varying the composition and ratio of metal precursor to semiconductor seeds in the synthesis, further enhancement in MOR activity could be expected. Additionally, an improved ORR semiconductor–metal system could potentially be designed in which the energy-level alignment would be favorable for the electron donation from the metal domain to the semiconductor domain. The semiconductor–metal nanocomposites could also be of interest as advanced functional materials and as catalysts for other reactions, such as organic and pharmaceuticals synthesis, environmental catalysis, photocatalysis, and oxidation/combustion reactions.

Received: February 17, 2011
Published online: April 14, 2011

Keywords: fuel cells · heterogeneous catalysis · nanocomposites · nanoparticles · semiconductors

[1] S. E. Habas, H. Lee, V. Radmilovic, G. A. Somorjai, P. Yang, *Nat. Mater.* **2007**, *6*, 692–697.
[2] J. Luo, L. Wang, D. Mott, P. N. Njoki, Y. Lin, T. He, Z. Xu, B. N. Wanjala, I. S. Lim, C. Zhong, *Adv. Mater.* **2008**, *20*, 4342–4347.
[3] S. H. Joo, J. Y. Park, C.-K. Tsung, Y. Yamada, P. Yang, G. A. Somorjai, *Nat. Mater.* **2009**, *8*, 126–131.
[4] W.-P. Zhou, X. Yang, M. B. Vukmirovic, B. E. Koel, J. Jiao, G. Peng, M. Mavrikakis, R. R. Adzic, *J. Am. Chem. Soc.* **2009**, *131*, 12755–12762.
[5] S. Sun, C. B. Murray, D. Weller, L. Folks, A. Moser, *Science* **2000**, *287*, 1989–1992.
[6] E. V. Shevchenko, D. V. Talapin, A. L. Rogach, A. Kornowski, M. Haase, H. Weller, *J. Am. Chem. Soc.* **2002**, *124*, 11480–11485.
[7] Z. Liu, J. E. Hu, Q. Wang, K. Gaskell, A. I. Frenkel, G. S. Jackson, B. Eichhorn, *J. Am. Chem. Soc.* **2009**, *131*, 6924–6925.
[8] J. Zhang, K. Sasaki, R. R. Adzic, *Science* **2007**, *315*, 220–222.
[9] S. Guo, S. Dong, E. Wang, *J. Phys. Chem. C* **2008**, *112*, 2389–2393.
[10] Y.-H. Chen, H.-H. Hung, M. H. Huang, *J. Am. Chem. Soc.* **2009**, *131*, 9114–9121.
[11] B. Lim, M. Jiang, P. H. C. Camargo, E. C. Cho, J. Tao, X. Lu, Y. Zhu, Y. Xia, *Science* **2009**, *324*, 1302–1305.
[12] H. Y. Lin, Y. F. Chen, *Appl. Phys. Lett.* **2006**, *88*, 161911.
[13] B. Kraeutler, A. J. Bard, *J. Am. Chem. Soc.* **1978**, *100*, 4317–4318.
[14] R. Baba, S. Nakabayashi, A. Fujishima, *J. Phys. Chem.* **1985**, *89*, 1902–1905.
[15] I. Pastoriza-Santos, D. S. Koktysh, A. A. Mamedov, M. Giersig, N. A. Kotov, L. M. Liz-Marzan, *Langmuir* **2000**, *16*, 2731–2735.
[16] N. Chandrasekharan, P. V. Kamat, *J. Phys. Chem. B* **2000**, *104*, 10851–10857.

 © 2011 Wiley-VCH Verlag GmbH & Co. KGaA, Weinheim

[17] V. Subramanian, E. Wolf, P. V. Kamat, *J. Phys. Chem. B* **2001**, *105*, 11439 – 11446.
[18] P. V. Kamat, *J. Phys. Chem. B* **2002**, *106*, 7729 – 7744.
[19] T. Hirakawa, P. V. Kamat, *J. Am. Chem. Soc.* **2005**, *127*, 3928 – 3934.
[20] M. Jakob, H. Levanon, *Nano Lett.* **2003**, *3*, 353 – 358.
[21] V. Subramanian, E. Wolf, P. V. Kamat, *J. Am. Chem. Soc.* **2005**, *126*, 4943 – 4950.
[22] T. Mokari, E. Rothenberg, I. Popov, R. Costi, U. Banin, *Science* **2004**, *304*, 1787 – 1790.
[23] T. Mokari, C. G. Sztrum, A. Salant, E. Rabani, U. Banin, *Nat. Mater.* **2005**, *4*, 855 – 863.
[24] C. Pacholski, A. Kornowski, H. Weller, *Angew. Chem.* **2004**, *116*, 4878 – 4881; *Angew. Chem. Int. Ed.* **2004**, *43*, 4774 – 4777.
[25] F.-R. Fan, Y. Ding, D.-Y. Liu, Z.-Q. Tian, Z. L. Wang, *J. Am. Chem. Soc.* **2009**, *131*, 12036 – 12037.
[26] A. E. Saunders, I. Popov, U. Banin, *J. Phys. Chem. B* **2006**, *110*, 25421 – 25429.
[27] G. Menagen, D. Mocatta, A. Salant, I. Popov, D. Dorfs, U. Banin, *Chem. Mater.* **2008**, *20*, 6900 – 6902.
[28] T. Mokari, A. Aharoni, I. Popov, U. Banin, *Angew. Chem.* **2006**, *118*, 8169 – 8173; *Angew. Chem. Int. Ed.* **2006**, *45*, 8001 – 8005.
[29] M. Casavola, V. Grillo, E. Carlino, C. Giannini, F. Gozzo, E. F. Pinel, M. A. Garcia, L. Manna, R. Cingolani, P. D. Cozzoli, *Nano Lett.* **2007**, *7*, 1386 – 1395.
[30] W. Shi, H. Zeng, Y. Sahoo, T. Y. Ohulchanskyy, Y. Ding, Z. L. Wang, M. Swihart, P. N. Prasad, *Nano Lett.* **2006**, *6*, 875 – 881.
[31] J. Yang, H. I. Elim, Q. Zhang, J. Y. Lee, W. Ji, *J. Am. Chem. Soc.* **2006**, *128*, 11921 – 11926.
[32] J. Yang, L. Levina, E. H. Sargent, S. O. Kelley, *J. Mater. Chem.* **2006**, *16*, 4025 – 4028.
[33] D. V. Talapin, H. Yu, E. V. Shevchenko, A. Lobo, C. B. Murray, *J. Phys. Chem. C* **2007**, *111*, 14049 – 14054.
[34] J.-S. Lee, E. V. Shevchenko, D. V. Talapin, *J. Am. Chem. Soc.* **2008**, *130*, 9673 – 9675.
[35] J. Yang, J. Y. Ying, *Chem. Commun.* **2009**, 3187 – 3189.
[36] H. Gu, R. Zheng, X. Zhang, B. Xu, *J. Am. Chem. Soc.* **2004**, *126*, 5664 – 5665.
[37] E. Elmalem, A. E. Saunders, R. Costi, A. Salant, U. Banin, *Adv. Mater.* **2008**, *20*, 4312 – 4317.
[38] S. E. Habas, P. Yang, T. Mokari, *J. Am. Chem. Soc.* **2008**, *130*, 3294 – 3295.
[39] I. Jen-La Plante, S. E. Habas, B. D. Yuhas, D. J. Gargas, T. Mokari, *Chem. Mater.* **2009**, *21*, 3662 – 3667.
[40] J. Yang, E. H. Sargent, S. O. Kelley, J. Y. Ying, *Nat. Mater.* **2009**, *8*, 683 – 689.
[41] L. L. Chng, J. Yang, Y. Wei, J. Y. Ying, *Adv. Synth. Catal.* **2009**, *351*, 2887 – 2896.
[42] V. Stamenkovic, T. J. Schmidt, P. N. Ross, N. M. Markovic, *J. Phys. Chem. B* **2002**, *106*, 11970 – 11979.
[43] Z. Liu, J. Y. Lee, M. Han, W. X. Chen, L. M. Gan, *J. Mater. Chem.* **2002**, *12*, 2453 – 2458.
[44] C. D. Wagner, A. V. Naumkin, A. Kraut-Vass, J. W. Allison, C. J. Powell, J. R. Rumble, Jr., *NIST Standard Reference Database 20*, Version 3.2 (Web Version).
[45] *Photochemical Conversion and Storage of Solar Energy* (Ed.: E. Pelizzetti, M. Schiavello), Springer, Berlin, **1990**.
[46] D. E. Eastman, *Phys. Rev. B* **1970**, *2*, 1 – 2.
[47] H. B. Michaelson, *J. Appl. Phys.* **1977**, *48*, 4729 – 4733.
[48] J. Hölzl, F. K. Schulte in *Solid Surface Physics* (Ed.: G. Höhler), Springer, Berlin, **1979**.
[49] R. Parsons, T. VanderNoot, *J. Electroanal. Chem.* **1988**, *257*, 9 – 45.
[50] F. A. Cotton, G. Wilkinson, *Advanced Inorganic Chemistry*, Wiley-Interscience, New York, **1980**.
[51] A. K. Shukla, A. S. Arico, K. M. El-Khatib, H. Kim, P. L. Antonucci, V. Antonucci, *Appl. Surf. Sci.* **1999**, *137*, 20 – 29.
[52] J. Yang, J. Y. Lee, H.-P. Too, S. Valiyaveettil, *J. Phys. Chem. B* **2006**, *110*, 125 – 129.
[53] A. S. Aricò, S. Srinivasan, V. Antonucci, *Fuel Cells* **2001**, *1*, 133 – 161.
[54] T. Toda, H. Igarashi, H. Uchida, M. Watanabe, *J. Electrochem. Soc.* **1999**, *146*, 3750 – 3756.

 © 2011 Wiley-VCH Verlag GmbH & Co. KGaA, Weinheim